



## A baseline Antarctic GIA correction for space gravimetry

Lambert Caron\*, Erik R. Ivins

*Jet Propulsion Laboratory, California Institute of Technology, Pasadena, CA, USA*



### ARTICLE INFO

#### Article history:

Received 30 October 2018

Received in revised form 26 October 2019

Accepted 6 November 2019

Available online 6 December 2019

Editor: B. Buffett

#### Keywords:

glacial isostatic adjustment

Antarctic mass trend

space gravimetry

Bayesian statistics

sea level

GRACE corrections

### ABSTRACT

Within the past decade, newly collected GPS data and geochronological constraints have resulted in refinement of glacial isostatic adjustment (GIA) models for Antarctica. These are critical to estimating and understanding ice mass changes at present-day. A correction needs to be made when using space gravity for ice mass balance assessments due to the fact that any vertical movements of the solid Earth masquerade as changes in ice mass, and these must be carefully removed. The main upshot of the new Antarctic GIA models is a downward revision of negative ice mass trends deduced from the Gravity Recovery and Climate Experiment (GRACE), resulting from a reduced GIA correction. This revision places GRACE inferred trend in mass balance within the one sigma uncertainty of mass balance deduced by altimetry. Because uncertainties in Holocene ice history and the low viscosity rheology beneath the West Antarctic Ice Sheet (WAIS) continue to vex further improvement in predictions of present-day GIA gravity rate, more emphasis has been given to regional-scale GIA models. Here we use a Bayesian method to explore the gravimetric GIA trend over Antarctica, both with and without the impact of a late Pleistocene Antarctic ice loads, along with the contribution of oceanic loads. We call this model without loads associated with Antarctica a baseline for regional GIA models to build upon. We consider variations of the radial mantle viscosity profile and the volume of continental-scale ice sheets during the last glacial cycle. The modeled baseline GIA is mainly controlled by the lower mantle viscosity and continental levering caused by ocean loading. We find that the predicted baseline GIA correction weakly depends on the ice history. This correction averages to +28.4 [16.5–41.9, 95% confidence] Gt/yr, of which  $+23.6 \pm 5.3$  are contributed by East Antarctica. In contrast, with late-Pleistocene Antarctic-proximal ice included, the total modeled mass trend due to GIA is +73.7 [30.1–114.7] Gt/yr. A baseline GIA correction of 28.4 Gt/yr is of order 50% of the mean net mass trend measured during the period 1992–2017. The statistical analysis provides tools for properly synthesizing any regional Antarctic GIA model with a self-consistent far-field component. This may prove important for accounting for both global and regional 3-D variations in mantle viscosity.

© 2019 Published by Elsevier B.V.

## 1. Introduction

Among the three methods employed for monitoring the decadal-time scale evolution of the Antarctic ice sheet, the Gravity Recovery And Climate Experiment (GRACE) mission has provided a very important contribution for the period between 2002 and 2017 (Tapley et al., 2019). In fact, analysis of this space gravimetric dataset now dominates the reports supplied to the recent IMBIE-2 Team (Shepherd et al., 2018) inter-comparison for Antarctic mass balance (see Extended Data figure 1 therein, in which almost 2/3 of the entries come from GRACE). GRACE analysis for Antarctica, however, come with one major caveat: a relatively poorly constrained glacial isostatic adjustment (GIA) model that must be used

to correct the trends recovered from the space gravimetric data (Whitehouse et al., 2019).

Estimates of present-day ice mass balance from GRACE data must be formulated as a subtraction of GIA model predicted gravity rates (also termed “GIA-correction”) from post-processed GRACE Level 2 data releases. Two facts make the GIA models problematic: significant regional deviation from the average upper mantle viscosity profile (O’Donnell et al., 2017) and the great ice cover over the continent. The latter hides geological data that could otherwise be used for understanding both the rebound processes and the paleo-geomorphological information that largely constrains ice history in Fennoscandia and Laurentia. Three types of data have emerged over that past 20 years that partially ameliorate these problems: Global Positioning System (GPS) station uplift data (Bevis et al., 2009), chronologically controlled methods for reconstructing the past expansion and fluctuation of the ice sheet both at its periphery (e.g. Anderson et al., 2014) and its vol-

\* Corresponding author.

E-mail address: [lambert.caron@jpl.nasa.gov](mailto:lambert.caron@jpl.nasa.gov) (L. Caron).

ume (e.g. Small et al., 2019). Collectively, these data have provided enough information that the total GIA corrections to the Antarctic mass trend, here noted  $\delta\dot{M}_T$ , have essentially more than halved from the time of the publication of the 1st inter-annual mass balance trend (Velicogna and Wahr, 2006). Ten years ago, some analyses found  $\delta\dot{M}_T$  corrections for GRACE with upper bounds in excess 275 Gt/yr (Bartlett et al., 2008). More recently, corrections as low as 33 Gt/yr have been plausibly extracted from better constrained models that employ the newly emerging geodetic (GPS) and geological data sets (see Schrama et al., 2014).

Some clues suggesting a minimal Antarctic ice advancement during the past several glacial maxima have come from deep ice core records (e.g. Lorius et al., 1984), revealing that cold and dry conditions in the interior compared to interglacial times. While such minimalist past ice reconstruction and subsequent land rebound are seemingly at odds with GPS uplift rates, that can regionally be near 8–9 mm/yr (Ivins et al., 2013; Argus et al., 2014), and some radiogenic dating suggesting 700-meter higher ice, even during the Holocene (Stone et al., 2003), it is clear that the Antarctic ice history remains shrouded by significant uncertainty, driving further revisions to current regional GIA models. Uncertainty in Late-Holocene atmospheric forcing may be even more important since seismic tomographic imaging data support viscoelastic models with an *a priori* low viscosity upper mantle, and reduced response time-scales (e.g. Nield et al., 2018) in West Antarctica. While ice core data reveal near continent-wide increases in snow fall during the last 1000 to 2000 years (Thomas et al., 2017; Stenni et al., 2017), the overall pattern of accumulation changes are controlled by the location of atmospheric pressure patterns over the adjacent oceans (Winstrup et al., 2019). The combination of the two effects both dampens rebound to unloading events occurring prior to 2 kyr, and may force the mantle to regionally subside (Ivins et al., 2000), potentially producing a more nuanced, and yet smaller, GIA correction for GRACE.

Given this new wrinkle in deriving optimal GIA corrections, we are motivated in this paper to bring clarity to the problem by carefully noting the significant participation of the lower mantle and the global nature of the GIA processes involved (Milne et al., 2009; Caron et al., 2018). Indeed, long-wavelength deformation, typically associated with the lower mantle and the vast global ocean loading, may link far-field ice history of the northern hemisphere ice sheets with part of the GIA signal in Antarctica. One important problem is that GIA models operate at various degree of regionality, and are not always able to constrain this long-wavelength deformation. To assess how significant that component is, we thus pose the question: what becomes of the GIA correction  $\delta\dot{M}_T$  in the absence of any direct contribution from the Antarctic ice sheet, and the sea-level changes induced by it? This latter hypothesis we refer to as the case of “No Antarctic loads”, or “NA”. We define this as a baseline GIA model for Antarctica. We will compare this model predicted  $\delta\dot{M}_{NA}$  mass correction to the case where ice sheets from both northern and southern hemisphere participate in the deglaciation, as is typical of fully global GIA models. The latter assumption will produce the total GIA correction,  $\delta\dot{M}_T$  that is associated with “fully global” GIA models that also incorporates Northern Hemispheric data (e.g., ICE-6G-VM5a and various relatives (see Argus et al., 2014; Peltier et al., 2015)).

## 2. State-of-the-art estimation of mass balance in the space observing era

### 2.1. Space gravimetry, altimetry and IOM

The GRACE contributions to the study of Antarctic ice change attribute most of the mass loss to West Antarctica (Shepherd et al., 2018; Tapley et al., 2019), and this is consistent with studies

using either altimetry or the input-output method (IOM). The latter methods allow a time series for mass change to be initiated near 1992. A summary of many recent advances in Antarctic GIA modeling can be found in Martín-Español et al. (2016) wherein the authors chose to compare physics-based model predictions to those reliant on data analysis. One technique recently in use is to combine altimetry and GRACE in the method described by Wahr et al. (2000) to solve for both GIA and ice mass trend. These lead to somewhat mixed results, however, as they must rely heavily on accurate bias corrections for altimetry and must deal with the error structure of the GRACE Level-2 spherical harmonic fields (Willen et al., 2019). A study by Gunter et al. (2014) found that Antarctic Ice Sheet (AIS) GIA solutions generated by this data-driven method gave mass-trend corrections in the range of 53 to 103 Gt/yr, with a large uncertainty ( $\pm 40$  Gt/yr). The importance of the GIA correction in the latter study for ice mass balance is critical, for within the period of observation, 2003–2009, when both ICESat-1 and GRACE data could be applied simultaneously, the total ice loss rate for AIS was estimated at  $-100 \pm 44$  Gt/yr.

### 2.2. Degree of regionality in GIA models

We distinguish three broad categories of GIA models suitable for GRACE corrections, each with its own advantages and drawbacks. First are fully global models, such as the ANU model (Lambeck et al., 2014), or the series of ICE-NG models (e.g. Argus et al., 2014; Peltier et al., 2015). These models treat the entire global data sets with full self-consistency and coupling, i.e., by solving the sea-level equation on the global scale (thus conserving total mass between the ocean and ice sheets at all model times) and taking into account the “far-field” long wavelength signal in Antarctica that originates mainly from changes in the Laurentide and Fennoscandian ice sheets, from the rotational feedback (e.g. Mitrovica et al., 2001), and from the far-field sea-level, in addition to the signal originating from Antarctic loads. The main downside of this category of models is that they are more inclined to compromise Antarctic ice history and preferred mantle viscosity to accommodate constraints in the far-field regions. In particular, fully global models have a tendency to invoke larger ice volume for the Antarctic ice sheet prior to the Holocene (Martín-Español et al., 2016), in order to meet far-field relative sea-level (RSL) constraints without increasing the volumes of the Laurentide and Fennoscandian ice sheets (cf. Carlson and Clark, 2012).

In contrast, regional models operate with various levels of approximation to the global part of the loading. We dub a second group as the fully regional models. These are based on empirically separating GIA from present-day sources in GPS, altimetry and gravimetry data using advanced data analysis techniques (e.g. Riva et al., 2009; Gunter et al., 2014; Martín-Español et al., 2016; Sasgen et al., 2018). While these models consistently include all of the Antarctic signal, so far no attempt has been made by such model to consider potential far-field sources in their interpretation of GIA, or to determine whether such GIA signal would be consistent with ice history or paleoshoreline data.

Quasi-global models operate somewhere in between the first two groups. These models can be either radially symmetric, such as IJ05\_R2 (Ivins et al., 2013), W12 (Whitehouse et al., 2012) and regionally-derived models (e.g. Bradley et al., 2015), or include lateral variations of the viscosity structure (Kaufmann et al., 2005; van der Wal et al., 2015; Gomez et al., 2018). The quasi-global models focus on varying the regional ice history and viscosity profile to best fit proximal constraints, including GPS, moraines and RSL indicators, while fixing the mass input to the oceans and using a fixed “background” northern hemisphere ice history (such as ICE-5G) to account for far-field signal. Like the fully regional models, they do not guarantee consistency with far-field RSL indicators

and do not examine other potential uncertainty and trade-offs related to far-field ice history.

It is important for regional-only AIS models of GIA to properly quantify the “far-field” influence and its uncertainty. To this extent our work presented in this paper provides important baseline information to be used in conjunction with these regionalized forward-modeling results. Our approach in this paper will be to make use of the increasingly voluminous global GPS and relative sea-level data that is available for constraining northern hemispheric ice to explore the consequences of the baseline “far-field” loading effects and their uncertainty. The analysis of this baseline GIA contribution is studied with Bayesian statistical rigor, treating both the data and parameter trade-offs that will dominate GIA corrections for time variable space gravimetric determinations of Antarctic mass balance. The results presented here may be used to complement future regional models. Key to our experiments is that we remove all assumed ice change proximal to Antarctica. We ask the question: to what extent is the far-field loading and response – and its uncertainty – an “Achilles Heel” of present Antarctic GIA correction modeling?

### 3. Methods

Here we employ methods developed by Caron et al. (2017, 2018), wherein a Bayesian approach using a Monte Carlo with Markov Chain (MCMC) computational strategy builds probability distribution functions from the data sets and model parameters. We perform the exploration of 3 structural parameters using a spherically-symmetric, compressible Maxwell Earth model: the lithospheric thickness, upper mantle viscosity and lower mantle viscosity, and 5 regional scaling coefficients for the ice history – applying to the North American Cordillera, Laurentide, Fennoscandia, Greenland and Antarctica – are varied, thus creating an ensemble of 64,000 forward GIA models. The scaled ice history is based on the ANU model in the northern hemisphere (Lambeck et al., 2014, e.g.) and the IJ05\_R2 model in Antarctica (Ivins et al., 2013), such that it is possible to directly link each scaling factor with a given ice volume of its corresponding ice sheet at all times, hence our choice of expressing these factors in terms of meter equivalent eustatic sea level (ESL) at the Last Glacial Maximum (LGM). The calculation accounts for rotational feedback, migrating coastlines arising as sea-level falls and rises, incorporating all the ancillary effects associated with solutions of the sea-level equation (SLE), including continental levering as, for example, described by Mitrovica et al. (2001). The SLE, and its associated gravity, sea-level and crustal deformation are computed on a  $1^\circ \times 1^\circ$  grid map, using spherical harmonics from degree 1 to 89 and a time step of 0.5 kyr. Note that our calculations are performed in the center-of-mass reference frame, so while the surface deformation and RSL possess a degree 1 component, gravity and mass trends do not, consistent with the lack of sensitivity to degree 1 by the GRACE observing system. Each forward model generates predictions that are compared to a global dataset assembling a) 11,451 RSL records covering the period 0–35 kyr BP and b) vertical land motion trends from 459 GPS sites. Each forward model is then assigned a probability value based on the Euclidean distance between the dataset values and the model predictions, along with weights that account for data uncertainty, balance between GPS and RSL sub-datasets, and bias caused by redundant information content (see Caron et al., 2017, 2018, for further details on this process). Together, all forward models of the ensemble create a probability density function (PDF) of GIA parameters and predicted signal, from which rigorous statistics such as expectation, standard deviation and confidence interval can be extracted.

**Table 1**

Components captured in the mass trends presented in this study. Note that continental loads refer to grounded ice in either or both Antarctica and non-Antarctic regions (i.e. Laurentide, Fennoscandia, Greenland, Patagonia and mountain glaciers), while oceanic loads refer to loads associated with the eustatic sea-level + relative sea level fingerprint contribution of the same regions considered.

Notation	Antarctic		Non-Antarctic	
	continental	oceanic	continental	oceanic
$\delta\dot{M}_T$	x	x	x	x
$\delta\dot{M}_{TC}$	x		x	
$\delta\dot{M}_{NA}$			x	x
$\delta\dot{M}_{AC}$	x			
$\delta\dot{M}_{AO}$		x		
$\delta\dot{M}_{NAC}$			x	
$\delta\dot{M}_{NAO}$				x

This PDF allows us to generate four statistical estimates of global GIA signal. First is the estimate that includes the signal generated by the total land ice and ocean mass changes during the last glacial cycle ( $T$  case), which comes directly from the model ensemble compared to the dataset used to establish the PDF (Caron et al., 2018). The contrasting case,  $NA$ , is obtained by removing from  $T$ , any GIA contribution owing to Antarctic ice loads, and any oceanic loads directly induced by them. What we mean by oceanic Antarctic load here is the contribution of the Antarctic ice sheet to the eustatic sea level curve, plus the relative sea-level fingerprint calculated via the SLE and associated with both this eustatic contribution and Antarctic ice history.

We can also isolate the non-Antarctic ocean loads, and total ocean loads using these separations. Hence we may, for example, also examine contributions to GIA corrections that arise from non-Antarctic continental ice ( $NAC$ ), or total continents ( $TC$ ). The components included in each of the mass trends are summarized in Table 1, along with the mass trends due to individual components from which we can obtain by linear combinations of  $\delta\dot{M}_T$ ,  $\delta\dot{M}_{TC}$ ,  $\delta\dot{M}_{NA}$  and  $\delta\dot{M}_{NAC}$ .

Fig. A.1 indicates the regions in green, yellow and red over the combination of which the signal is integrated to obtain the total mass trend over Antarctica: this area was chosen to encompass all points of Antarctica above present-day sea level (excluding ice shelves) as well as all points within 150 km of this grounding line. The method is nearly identical to that employed in Shepherd et al. (2012) and Velicogna and Wahr (2013).

### 4. Results and discussion

Fig. 1 maps the expected GIA mass trend for all four separation cases considered. Frame 1c ( $T$ ) is identical to the rates reported in Caron et al. (2018), predicting near-zeros mass trends in the interior of East Antarctica, positive mass trends over Ellsworth Land, Ross Ice Shelf and coastal regions of the continent, surrounded by a forebulge with negative mass trends. Frame 1a shows a similar case, but excluding oceanic loading ( $TC$ ). The coastal regions appear similar, but the interior of East Antarctica and eastern Antarctic ocean see slightly negative trends, while the western ocean sees slightly positive trends. This east-west gradient is clearly highlighted in frame 1b which shows the signal due to far-field ice only ( $NAC$ ), and is, in fact, dominated by the degree 2, order 1 coefficients (see Figs. A.6 and A.7), which is related to rotational feedback. The signal in frame 1d ( $NA$  case) essentially conforms to an outline of Antarctica, with a remarkably uniform signal within the continent, not unlike that of Australia in traditional global GIA models (Kendall et al., 2005). The contrast with the surrounding oceanic area, having lower predicted rates, is due to sea-level loading of the oceanic floor during the deglaciation period and

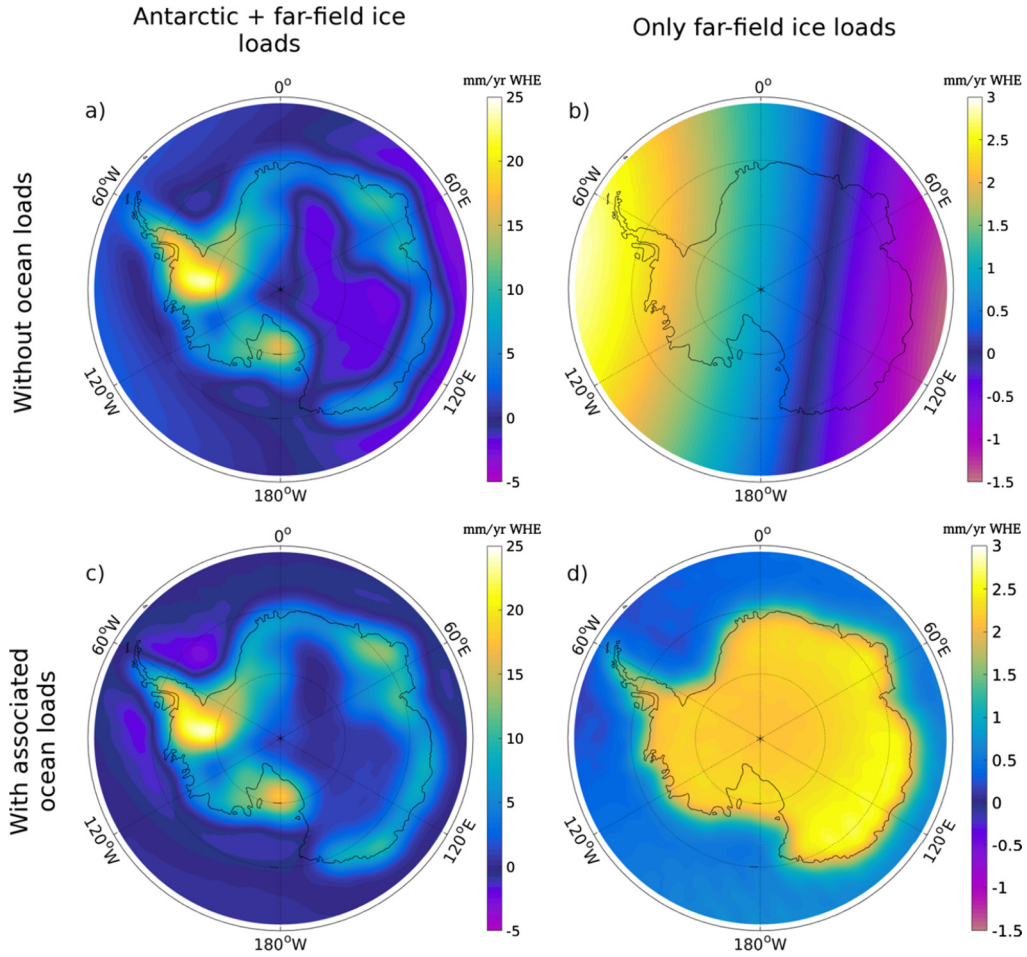


**Fig. 1.** Maps of gravity trends expectation over Antarctica. a) Case with both far-field and Antarctic ice loads and without ocean loads (TC), b) case with far-field ice loads only and without ocean loads (NAC), c) case with both far-field and Antarctic ice loads, with all associated ocean loads ( $T$ ), d) case with far-field ice loads and their associated ocean loads only (NA). Note that in the NA and NAC cases the amplitude is smaller than  $T$  and TC, with relatively more energy in the long wavelengths. (For interpretation of the colors in the figures, the reader is referred to the web version of this article.)

subsequent times. Sea-level loading around Antarctica has the effect of creating “reverse forebulge” deep into the continent, while pushing up coastal area as the lithosphere beneath the sea floor subsides. This deformation is sometimes referred to as continental levering (Mitrovica et al., 2001). In frame 1d, the combination of ocean loading and self-gravitation overwhelms the amplitude of the far-field continental loading effects in Antarctica. The east-west gradient essentially vanishes, and has even slightly been reversed. Self-attraction is accounted for in the SLE, and the effect is to lower sea-level in regions of low gravity and raise it in regions of high gravity. Thus, this additional water load forces subsidence of the seafloor beneath and adjacent to the West Antarctic Ice Sheet (WAIS), and uplift beneath the East Antarctic Ice Sheet (EAIS), causing solid-earth mass changes opposite to that of Fig. 1b. The effect, ultimately, is to homogenize the predicted far-field GIA mass trends in Antarctica, as in Fig. 1d. This is consistent with earlier work showing that GRACE mass balance estimates for Antarctica are sensitive to low degree coefficients (Chen et al., 2008; Schrama et al., 2014) but less to the degree 2 order 1 coefficients (van der Wal et al., 2015). The uncertainties of these quantities shown in Fig. 1 are mapped in Fig. 2. An alternative decomposition of component contributions is also possible. In contrast to Fig. 1, individual components consisting of gravity signal due to Antarctic continental loads  $AC$ , Antarctic oceanic loads  $AO$ , non-Antarctic continental loads  $NAC$  and non-Antarctic oceanic loads  $NAO$ , are mapped in Fig. A.5.

Fig. 3 shows the pattern of mass trends for 12 different forward models parametrized with varying viscosity profile. Fig. 3 also shows the expected values for the other parameters,  $T_e = 108.5$  km, and the model masses of the continental ice sheets at LGM in meters ESL:  $\alpha_C = 7.5$  m,  $\alpha_L = 76.2$  m,  $\alpha_F = 23.9$  m and  $\alpha_G = 6.3$  m (also see Table 2). The first effect to be noted is that the amplitude peaks at intermediate values of the lower mantle viscosity, diminishes for low viscosity, and finds intermediate values for high viscosity. Secondly, Fig. 3 reveals that the peak of the signal migrates from the interior beneath EAIS to coastal regions as the upper mantle viscosity increases, with relatively little influence on the average continental signal. With comparable Earth structure parameters, Fleming et al. (2012) found levering predictions for the Australian continent similar to that shown here in frames (b) and (e) of Fig. 3. A cause for the near-uniform expected gravity rate pattern is, therefore, that the complementary patterns of low and high upper mantle viscosity models tend to compensate one another in the model ensemble derived average positive trend pattern. This result is especially important, as we compute the far-field influence on East Antarctic GIA to be statistically dominated by long wavelengths, and therefore might not be so easily captured in data combination methods. GIA in this vast region is essential to the issue of correctly recovering the present-day mass balance of the EAIS (Martin-Español et al., 2017; Willen et al., 2019).

Fig. 4 displays the essential PDF retrieved for the AIS using our Bayesian MCMC computations. The ordinate axes all show the total

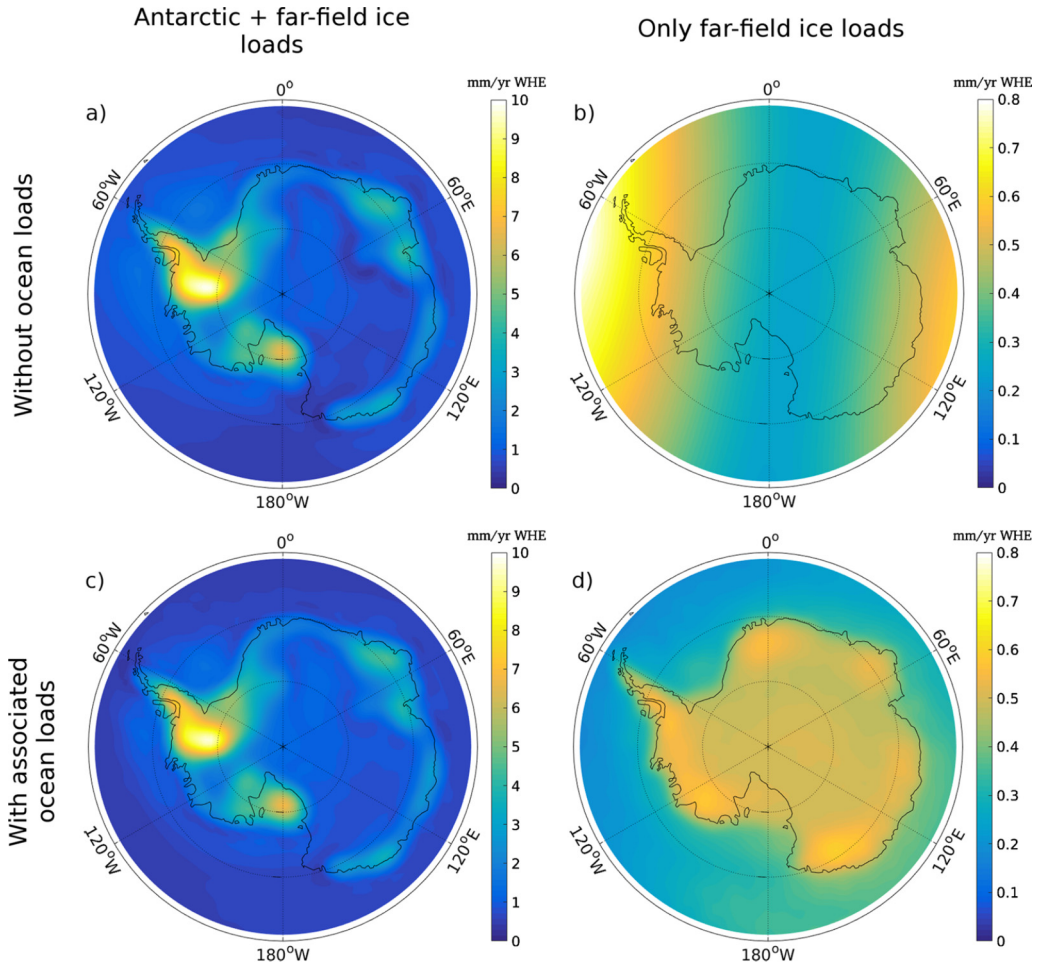


**Fig. 2.** Maps of the standard deviation of gravity trends over Antarctica. a) Case with both far-field and Antarctic ice loads and without ocean loads ( $T_C$ ), b) case with far-field ice loads only and without ocean loads ( $NAC$ ), c) case with both far-field and Antarctic ice loads, with all associated ocean loads ( $T$ ), d) case with far-field ice loads and their associated ocean loads only ( $NA$ ).

**Table 2**

Parameters and mass trends over Antarctica.  $\eta_{UM}$ : upper mantle viscosity ( $\log_{10}(\text{Pas})$ ),  $\eta_{LM}$ : lower mantle viscosity ( $\log_{10}(\text{Pas})$ ),  $T_e$ : elastic lithosphere thickness (km),  $\alpha_C, \alpha_L, \alpha_F, \alpha_A, \alpha_G$ : regional ice scaling coefficients for the Cordilleran, Laurentide, Fennoscandian, Antarctic and Greenland ice sheets, respectively (m equivalent ESL at the LGM). GIA mass trends over Antarctica are expressed in Gt/yr.

Parameter	Best fit	expectation ± standard deviation	95% confidence interval
$\eta_{UM}$	20.61	20.78 ±0.2253	[20.51, 21.32]
$\eta_{LM}$	21.77	22.34 ±0.5169	[21.5, 23.52]
$T_e$	91.03	108.5 ±31.59	[66.7, 184.5]
$\alpha_C$	6.443	7.545 ±4.214	[1.678, 18.88]
$\alpha_L$	66.18	76.15 ±13.43	[57.99, 109.1]
$\alpha_F$	19.79	23.88 ±6.217	[17.75, 40.21]
$\alpha_A$	9.126	8.251 ±2.912	[2.467, 14.53]
$\alpha_G$	6.527	6.345 ±2.983	[1.455, 13.84]
$\delta\dot{M}_{TC}$	65.67	50.73 ±19.98	[13.35, 88.97]
$\delta\dot{M}_T$	87.54	74.2 ±21.64	[30.09, 114.7]
$\delta\dot{M}_{NAC}$	2.782	5.894 ±3.302	[1.544, 11.86]
$\delta\dot{M}_{NA}$	23.22	28.44 ±6.471	[16.46, 41.87]
$\delta\dot{M}_{AC}$	62.89	44.83 ±21.24	[7.391, 85.2]
$\delta\dot{M}_{AO}$	1.423	0.9241 ±0.6671	[-0.1798, 2.257]
$\delta\dot{M}_{NAC}$	2.782	5.894 ±3.302	[1.544, 11.86]
$\delta\dot{M}_{NAO}$	20.44	22.55 ±4.248	[14.31, 31.7]

mass rate that is deduced from our masking procedure versus all input parameters of the model inversion (abscissa). Fig. A.4 shows

the PDF where the mass trends are split up by individual components instead. The resultant statistics are summarized in Table 2. Further analysis for the subregions of East Antarctica, West Antarctica and the Antarctic Peninsula are available in Appendix Figs. A.2, A.3 and Table A.1. Note that a total of about  $+28.4 \pm 6.5$  Gt/yr is expected over Antarctica in the  $NA$  case versus  $+73.7 \pm 21.6$  Gt/yr for the  $T$  case. From Table 2 we can see that about 80% of the former mass trend is attributed to oceanic loading associated with far-field ice sheets ( $\delta\dot{M}_{NAO} = 22.55 \pm 4.25$  Gt/yr), with the remainder caused by far-field ice sheet loading alone ( $\delta\dot{M}_{NAC} = 5.89 \pm 3.30$  Gt/yr). In other words,  $\delta\dot{M}_{NA}$  is sensitive to the melt-water curve but less so to the distribution of the ice sheets themselves. By contrast, ocean loading associated with the AIS ( $\delta\dot{M}_{AO}$ ) contributes less than 1 Gt/yr to the total mass trend ( $\delta\dot{M}_T$ ). This is negligible compared to the contribution of continental Antarctic loading and its uncertainty ( $\delta\dot{M}_{AC} = 44.83 \pm 21.24$  Gt/yr). The latter finding is important for regional Antarctic models, because it means that the integration of the baseline GIA correction is essentially the same whether or not it includes ocean loading generated by Antarctica, making it independent of the choice of Antarctic ice history. We find that this conclusion holds true even for regional mass trends, with the  $AO$  component amounting to less than 2% of the total mass trend in every region considered in this study. Note that all 4 individual components  $\delta\dot{M}_{AC}$ ,  $\delta\dot{M}_{AO}$ ,  $\delta\dot{M}_{NAC}$  and  $\delta\dot{M}_{NAO}$  have a positive average contribution to  $\delta\dot{M}_T$  on the continental scale.

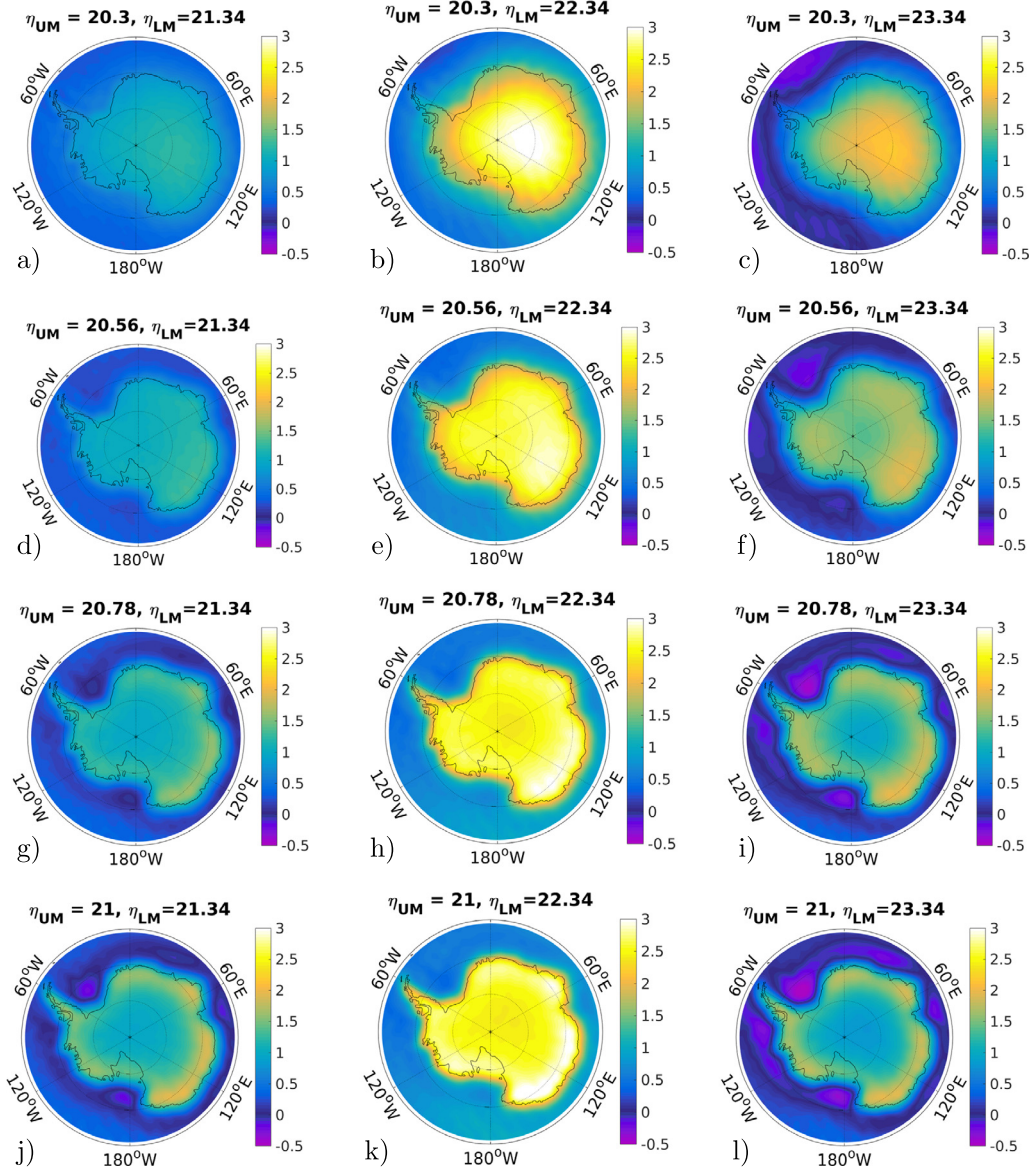


**Fig. 3.** Gravity trend (mm/yr water height equivalent) in the NA case for GIA models with different viscosity profiles. The other parameters are identical in each case and equal to the expected values as displayed in Table 2. The amplitude is maximum in the interior for intermediate values of the lower mantle viscosity, while continental levering increases with the upper mantle viscosity, localizing the signal near the coast. The model in the central column, third row corresponds to the model with expected parameter values. (Viscosity values are in  $\log_{10}$  units Pas, as in Table 1.)

While the IMBIE-2 study reports a trend of  $-109 \pm 56$  Gt/yr for Antarctica for the period 1992–2017, the net space gravimetry result for 2003–2010 is  $-76 \pm 20$  Gt/yr, and uncorrected for GIA stands at  $-22 \pm 9$  Gt/yr. The point here is that our baseline expectation for far field and ocean-related GIA correction (NA case) is roughly 50% of the GIA correction applied in the IMBIE-2 study and roughly equal in magnitude to the GRACE trend recovered directly from gravity changes determined for 2003–2010. The baseline result is a surprisingly large correction, given the maximum amplitude of the signal, and clearly related to the value of the modeled lower mantle viscosity. It is important to remember that the mass trends are dependent on the mask on which they are integrated, especially when long wavelength dominate the signal.

Highlighted in Fig. 4 is the fact that for the T and TC case the Antarctic scaling coefficient ( $\alpha_A$ ) is the main controlling parameter of the mass trend. The relation appears to be nearly linear, which simply reflects the linear relationship between defor-

mation and surface loading. However, note that fitting a straight line through the high probability region of  $\delta\dot{M}_T$  versus  $\alpha_A$  in Fig. 4 would not intersect the vertical axis at the origin. Indeed, when  $\alpha_A \rightarrow 0$ ,  $\delta\dot{M}_T \rightarrow \delta\dot{M}_{NA}$ , and similarly for  $\delta\dot{M}_{TC} \rightarrow \delta\dot{M}_{NAC}$ .

It is easily deduced from the first and third rows of Fig. 4 that the NA mass trend  $\delta\dot{M}_{NA}$  exhibits a large (albeit non-linear) correlation to  $\eta_{LM}$ , more so than to any other parameter. The correlation is even stronger in the NAC case. There is much coherency in this sensitive relationship: this explains why the signal is nearly uniform over Antarctica, as lower mantle deformation is associated with the long wavelengths. Here we can find another reason for the uniformity of the expected gravity rates over the continent: the high probability region is centered around  $\eta_{UM} = 20.8$ ,  $\eta_{LM} = 22.3$ , and these values produce high, uniform positive rates (also see Fig. 3). Non-uniform predictions are to some degree weighted out in the statistics by their relatively lower probability.

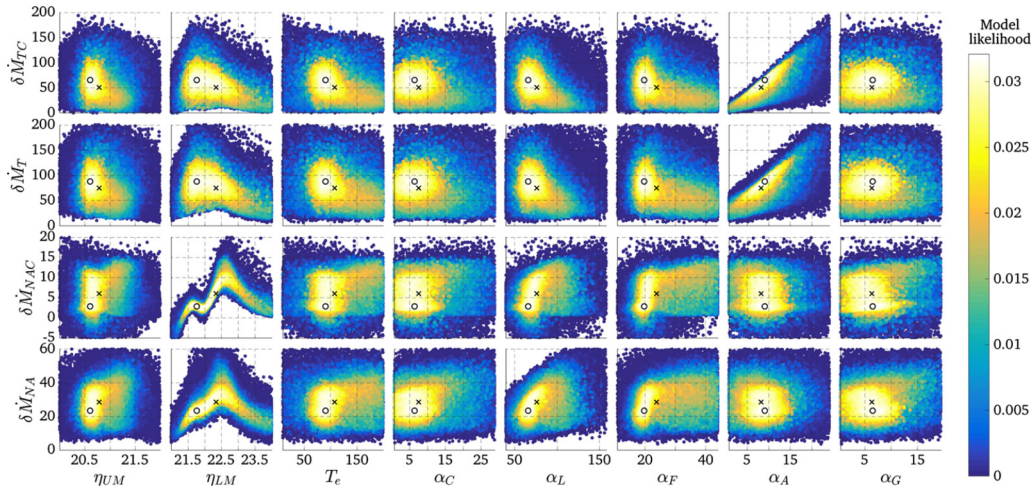


**Fig. 4.** Likelihood probability plotted against predicted Antarctic mass trends  $\delta\dot{M}_{NAC}$ ,  $\delta\dot{M}_{TC}$ ,  $\delta\dot{M}_{NA}$  and  $\delta\dot{M}_T$  (in Gt/yr) and every variable parameter used in this study:  $\eta_{UM}$ ,  $\eta_{LM}$ : logarithm of the upper and lower mantle viscosities ( $\log_{10}(\text{Pa s})$ ), respectively,  $T_e$ : thickness of the lithosphere (km),  $\alpha_C$ ,  $\alpha_L$ ,  $\alpha_F$ ,  $\alpha_A$ ,  $\alpha_G$ : scaling factors for the Cordilleran, Laurentide, Fennoscandian, Antarctic and Greenland ice sheets, respectively (m eustatic sea level equivalent at the LGM). The black circle and black cross indicate the best-fitting and expected parameter values, respectively. Note that models with higher probability are plotted on top of and thus may mask from view models with lower probability.

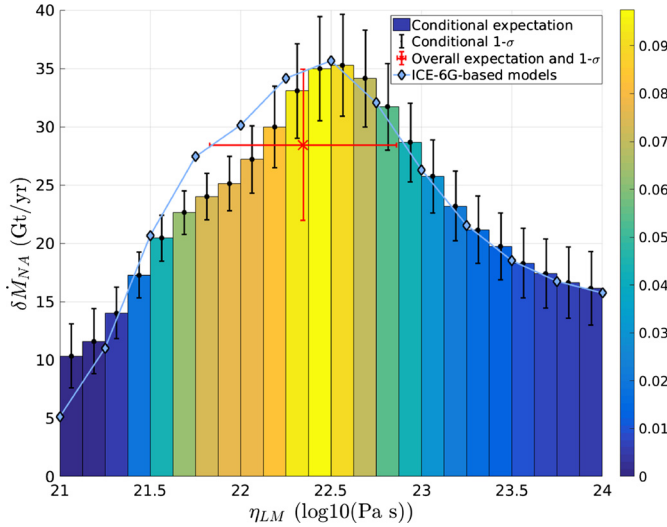


**Fig. 5.** Mass trends as a function of the lower mantle viscosity for the NA case. The model ensemble is divided into intervals of  $0.125 \log_{10}(\text{Pa s})$ . In each interval the recorded expectation (as measured by the height of the bars) and standard deviation (black error bars) of the mass trend is shown. These values are also reported in Table A.2. The red marker with error bars indicate the expectation and standard deviation of the overall distribution, while the bar colors reflect the marginal likelihood of  $\eta_{LM}$  for each interval. The light blue line is the mass trend resulting from assuming the a priori ICE-6G ice loading as the starting model (unscaled), a lithospheric thickness of 100 km, an upper mantle viscosity of  $10^{20.8} = 6.3 \times 10^{20} \text{ Pa s}$ , and variable lower mantle viscosity.

Fig. 5 illustrates the NA mass trend versus lower mantle viscosity relationship in greater detail, illuminating the statistics over sub-samples of the distribution at each 0.125 interval of  $21 \leq \eta_{LM} \leq 24$ . Bin heights show the expected mass trend over the Antarctic continent for each interval with the associated standard deviation (black error bars). Bar colors indicate the marginal probability of each interval, in other words, the likelihood that this particular range of lower mantle viscosity is to fit our data set with all variations of the other parameters accounted for. In fact, this can be thought of as the weight of each interval to our overall statistics. The red cross and error bars in Fig. 5 indicate the overall expectation and standard deviation of the lower mantle viscosity and mass trend in the NA case. Although, in principle, using a different

dataset or ice model could lead to a somewhat different marginal probability, we expect the overall  $\delta\dot{M}_{NA}$  dependence on  $\eta_{LM}$  to be quite robust. We verified this by generating a series of forward models (light blue curve) with ICE-6G as the far-field model, a 100 km lithosphere, an upper mantle viscosity of  $6.3 \times 10^{20} \text{ Pa s}$  and a lower mantle with varying viscosity. Using these interrelationships for  $\delta\dot{M}_{NA}$ , future generations of regional-only GIA models can derive a far-field correction to Antarctic mass trend that is consistent with their choice of lower mantle viscosity, should it be different from our expected value. The relationship is therefore of value for developing refined continent-wide finite element models that consider the sharp contrasts in lithospheric thickness and mantle viscosity that characterize the differences between east and west Antarctica along the spine of the Transantarctic Mountains. The  $\delta\dot{M}_{NA}$  results reported can supplement the GIA-corrective trends extracted with continental-scale ice sheet flow models that actually have regional viscoelastic isostatic responses computed, such as in the ensemble study of Briggs et al. (2013).

Other positive correlations, though of secondary importance, appear in the NA case between the total GIA mass trend and the ice volume in Fennoscandia and Laurentia ( $\alpha_F$  and  $\alpha_L$ , respectively). This is expected, as these two ice sheets, and the oceanic loading they produce, are the main sources of Antarctic proximal signal, in the absence of Antarctic ice loads.

We note the possible influence of lateral variations of the viscosity and lithospheric structure on our computed mass trends, as our model uses a 1-D radial viscosity profile. Given the much higher vertical land motion observed by GPS (Barletta et al., 2018) than calculated from our global models in the coastal Amundsen Sea sector, we can expect the contribution of that region to be underestimated in the T case. However, we find the NA case to be driven by the lower mantle, and given that low viscosity anomalies may diminish below 800 km depth (Hansen et al., 2014; Lloyd et al., 2019), potential bias from not accounting for lateral heterogeneity is likely minimal over land, where our integration is performed. However, adequate modeling of the low viscosity oceanic region surrounding Antarctica could change the map of gravity trends immediately adjacent to the continent (Kaufmann et al., 2005; Whitehouse et al., 2019). In light of the results shown in Fig. 3, we could expect a smooth gradient between oceanic and continental gravity rates, given the probabilities of  $\eta_{LM}$  and  $\eta_{UM}$  shown in Fig. 4.

## 5. Conclusion

We have derived a statistical estimate of the GIA signal in Antarctica due to ocean and far-field ice sheet changes. The far-field histories for the last of the Late-Pleistocene glacial terminations are well constrained by data, as are the solid-Earth viscoelastic response in the Northern Hemisphere. We can therefore use the statistics derived here, which have emphasized models of the more tightly constrained Northern Hemisphere, to offer a baseline GIA correction for all space gravimetric inferences of Antarctic ice mass balance, including those that come from tracking multiple satellites at higher orbital altitude than GRACE (Sośnicka et al., 2012; Bonin et al., 2018). Further research is necessary for establishing this baseline as a viable lower bound, however.

We find that the baseline GIA contribution to present-day mass trend correction ( $\delta\dot{M}_{NA}$ ) amounts to a significant part of the trend deduced from GRACE Level 2 data products. The correction contributes a  $28.4 \pm 6.5$  Gt/yr to the estimation of mass change over the continent, around 80% of which is generated by oceanic loading related to far-field ice sheets. This is to be contrasted with the current estimated correction of  $73.7 \pm 21.6$  Gt/yr when we include the ice loading history interior to, and immediately offshore of, an LGM and post-LGM evolving Antarctic ice sheet. The expected baseline GIA gravity signal is quasi-uniform over the continent, owing to the balance of the large scale signal from the far-field ice sheets and the continental levering caused by rising sea-level during global deglaciation. Given its surface area, solid Earth GIA beneath the EAIS is predicted to be the biggest contributor to this baseline mass trend. In our model ensemble, the resulting continental mass trend associated with our newly derived baseline GIA correction is primarily controlled by the lower mantle viscosity, with relatively little impact from the upper mantle viscosity. Further work involving GIA models with laterally-varying viscosity is needed to determine if any significant sensitivity to the upper mantle viscosity would appear in the presence of the strong lateral heterogeneity structure known to exist between west and east Antarctica, especially as this could affect the correlations between the NA signal and scaling of ice sheets. Here we have presented a statistical quantification of this dependency on the lower mantle viscosity that can be utilized in future regionally-focused GIA models of Antarctica.

## Declaration of competing interest

The authors declare that they have no known competing financial interests or personal relationships that could have appeared to influence the work reported in this paper.

## Acknowledgements

This research was carried out at the Jet Propulsion Laboratory (JPL), California Institute of Technology, under a contract with the National Aeronautics and Space Administration (NASA). We thank one anonymous reviewer for their insightful suggestions and comments. We thank sponsors: the NASA Post-doctoral Program and ROSES funds for the GRACE Science Team (grant #967701.02.03.01.81), Cryosphere Program (grant #967701.02.03.01.30), NASA Sea-level Change Team (grants #509496.02.08.10.65 and 16-SLCT16-0015; 2018–2020) and Earth Surface and Interior Focus Areas (grant #281945.02.47.03.86). Spherical harmonic computations were performed using SHTOOLS (Wieczorek et al., 2016). We thank Kurt Lambeck and Anthony Purcell for providing the ANU model and part of our RSL compilation. Statistics on present-day Antarctic GIA gravity rates derived from this study are available at <https://vesl.jpl.nasa.gov/solid-earth/gia>.

## Appendix A. Mass trends for the subregions of East Antarctica, West Antarctica and the Antarctic Peninsula

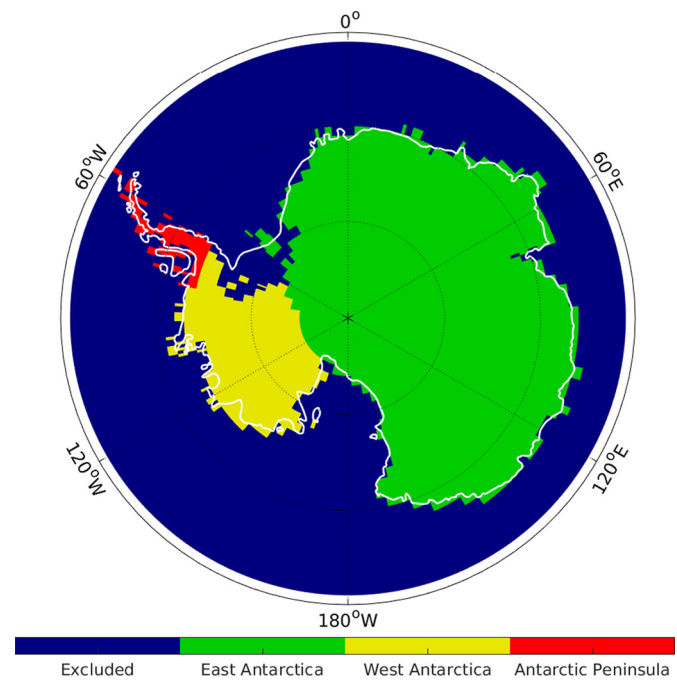


**Fig. A.1.** Maps of the masks used to integrate mass trends in Antarctica. Mass trends reported in the main text result from the integration over the combined area of all three subregions.

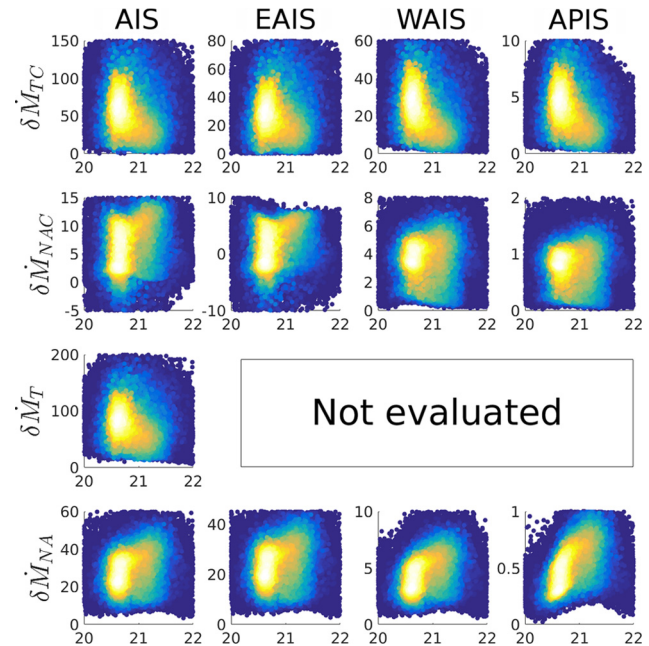


**Fig. A.2.** Probability density function, plotted as a function of the mass trends (y-axis, Gt/yr) and upper mantle viscosity  $\eta_{UM}$  (x-axis,  $\log_{10}(\text{Pa s})$ ) for different regions, similarly to Fig. 4. Note that, in the NAC and NA cases, even though a higher upper mantle viscosity focuses the signal on coastal areas such as the Antarctic Peninsula, none of the cases evaluated shows significant sensitivity to the upper mantle viscosity. In the T case, the mass trends of individual models of the ensemble were only kept for the combined mask of all regions, hence the plots for subregions are missing. Given the large correlation with the TC case however, we assume the values would look similar to those of TC, only with amplitude about 50% larger.

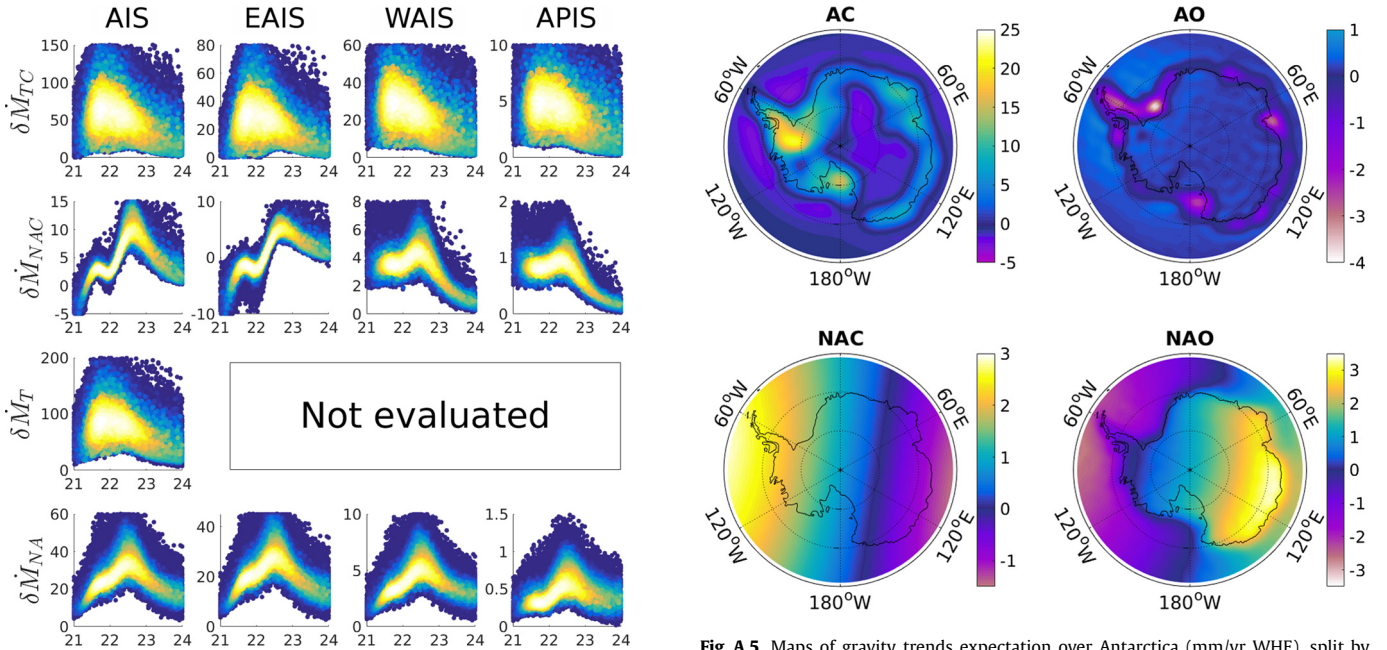


**Fig. A.3.** Probability density function, plotted as a function of the mass trends (y-axis, Gt/yr) and lower mantle viscosity  $\eta_{LM}$  (x-axis,  $\log_{10}(\text{Pa s})$ ) for different regions, similarly to Fig. 4. Note that, in the NAC and NA cases, even though a higher upper mantle viscosity focuses the signal on coastal areas such as the Antarctic Peninsula, the primary influence remains the lower mantle viscosity in all regions. In the  $T$  case, the mass trends of individual models of the ensemble were only kept for the combined mask of all regions, hence the plots for subregions are missing. Given the large correlation with the  $TC$  case however, we assume the values would look similar to those of  $TC$ , only with amplitude about 50% larger.

**Fig. A.5.** Maps of gravity trends expectation over Antarctica (mm/yr WHE), split by individual component:  $AC$  = Antarctic continental forcing,  $AO$  = Antarctic oceanic forcing,  $NAC$  = Non-Antarctic continental forcing,  $NAO$  = Non-Antarctic oceanic forcing.

**Table A.1**

Expectation of the integrated mass trends (Gt/yr) on, and surface area of ( $\times 10^6 \text{ km}^2$ ) different masks. EAIS: East Antarctic Ice Sheet, WAIS: West Antarctic Ice Sheet, APIS: Antarctic Peninsula Ice Sheet, AIS: Antarctic Ice Sheet.

Mask	Surface area	$\delta\dot{M}_{NAC}$	$\delta\dot{M}_{NA}$	$\delta\dot{M}_{TC}$	$\delta\dot{M}_T$
EAIS	11.119	$1.35 \pm 2.96$	$23.59 \pm 5.28$	$24.68 \pm 9.96$	$47.57 \pm 12.47$
WAIS	2.1413	$3.72 \pm 0.91$	$4.37 \pm 1.09$	$22.10 \pm 8.95$	$22.90 \pm 8.43$
APIS	0.3366	$0.82 \pm 0.21$	$0.486 \pm 0.149$	$3.95 \pm 1.45$	$3.28 \pm 1.27$
AIS	13.597	$5.89 \pm 3.30$	$28.44 \pm 6.47$	$50.72 \pm 19.98$	$73.75 \pm 21.43$

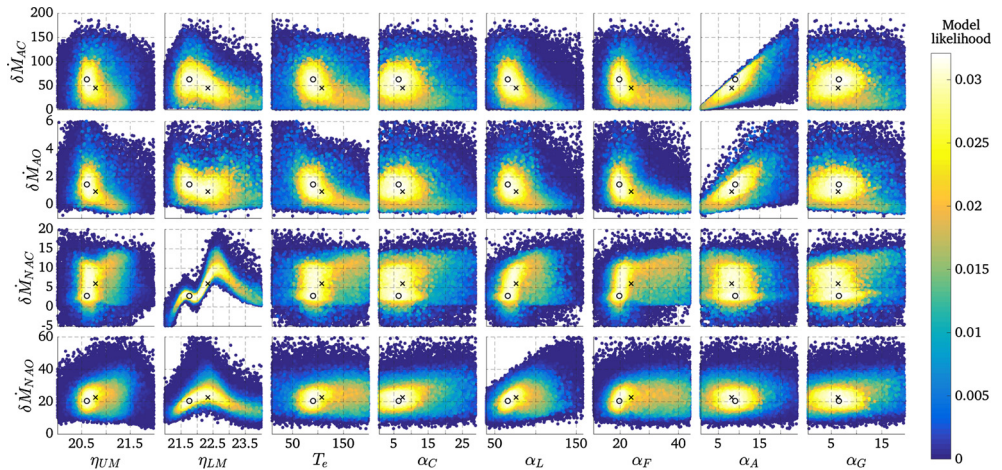


**Fig. A.4.** Likelihood probability plotted against predicted Antarctic mass trends  $\delta\dot{M}_{NAC}$ ,  $\delta\dot{M}_{AC} = \delta\dot{M}_{TC} - \delta\dot{M}_{NAC}$ ,  $\delta\dot{M}_{NAO} = \delta\dot{M}_{NA} - \delta\dot{M}_{NAC}$  and  $\delta\dot{M}_{AO} = \delta\dot{M}_T - \delta\dot{M}_{TC} - \delta\dot{M}_{NAO}$  (in Gt/yr) and every variable parameter used in this study:  $\eta_{UM}$ ,  $\eta_{LM}$ : logarithm of the upper and lower mantle viscosities ( $\log_{10}(\text{Pas})$ ), respectively,  $T_e$ : thickness of the lithosphere (km),  $\alpha_C$ ,  $\alpha_L$ ,  $\alpha_F$ ,  $\alpha_A$ ,  $\alpha_G$ : scaling factors for the Cordilleran, Laurentide, Fennoscandian, Antarctic and Greenland ice sheets, respectively (m eustatic sea level equivalent at the LGM). The black circle and black cross indicate the best-fitting and expected parameter values, respectively. Note that models with higher probability are plotted on top of and thus may mask from view models with lower probability.

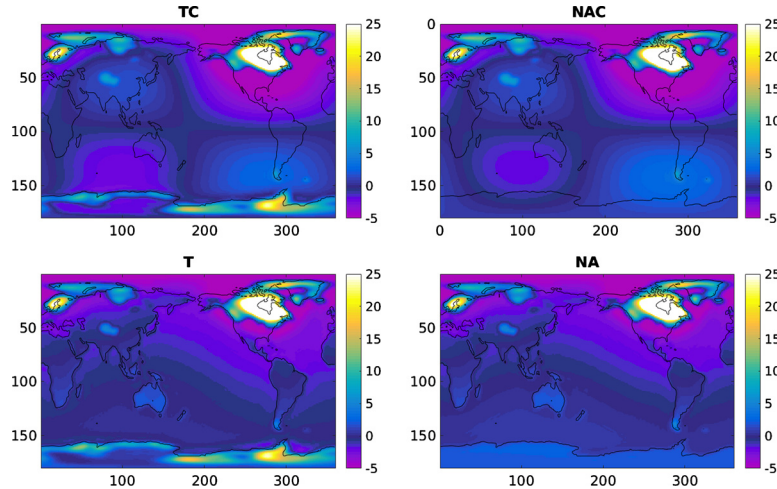


**Fig. A.6.** Maps of gravity trends expectation (mm/yr WHE), same results as Fig. 1, but with a global view.

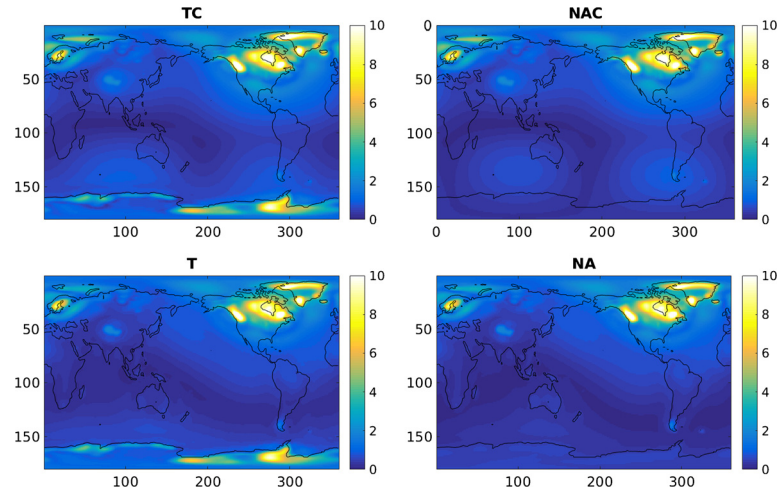


**Fig. A.7.** Maps of the standard deviation of gravity trends (mm/yr WHE), same results as Fig. 2 but with a global view.

**Table A.2**

Conditional expectation and standard deviation of  $\delta\dot{M}_{NA}$  (Gt/yr) upon the choice of a lower mantle viscosity interval ( $\log_{10}$  Pas).

$\eta_{LM}$ interval	$\delta\dot{M}_{NA}$ expectation $\pm 1\sigma$	Marginal probability
21.000–21.125	10.335 $\pm$ 2.726	2.985e-04
21.125–21.250	11.594 $\pm$ 2.795	1.032e-03
21.250–21.375	14.021 $\pm$ 2.222	4.764e-03
21.375–21.500	17.281 $\pm$ 1.988	1.855e-02
21.500–21.625	20.441 $\pm$ 1.959	4.359e-02
21.625–21.750	22.624 $\pm$ 1.872	6.308e-02
21.750–21.875	23.999 $\pm$ 1.972	7.404e-02
21.875–22.000	25.115 $\pm$ 2.342	7.707e-02
22.000–22.125	27.186 $\pm$ 2.888	7.835e-02
22.125–22.250	29.972 $\pm$ 3.476	8.364e-02
22.250–22.375	33.074 $\pm$ 4.057	9.468e-02
22.375–22.500	34.976 $\pm$ 4.459	9.756e-02
22.500–22.625	35.266 $\pm$ 4.370	9.054e-02
22.625–22.750	34.145 $\pm$ 4.152	7.016e-02
22.750–22.875	31.709 $\pm$ 3.717	5.425e-02
22.875–23.000	28.642 $\pm$ 3.363	4.287e-02
23.000–23.125	25.732 $\pm$ 3.123	2.966e-02
23.125–23.250	23.198 $\pm$ 2.981	2.142e-02
23.250–23.375	21.160 $\pm$ 2.905	1.570e-02
23.375–23.500	19.756 $\pm$ 2.865	1.250e-02
23.500–23.625	18.295 $\pm$ 3.003	9.064e-03
23.625–23.750	17.393 $\pm$ 2.965	6.789e-03
23.750–23.875	16.625 $\pm$ 3.069	5.880e-03
23.875–24.000	16.141 $\pm$ 3.140	4.526e-03

## References

- Anderson, J.B., Conway, H., Bart, P.J., Witus, A.E., Greenwood, S.L., McKay, R.M., Hall, B.L., Ackert, R.P., Licht, K., Jakobsson, M., et al., 2014. Ross Sea paleo-ice sheet drainage and deglacial history during and since the LGM. *Quat. Sci. Rev.* 100, 31–54.
- Argus, D.F., Peltier, W., Drummond, R., Moore, A.W., 2014. The Antarctica component of postglacial rebound model ICE-6G\_C (VM5a) based on GPS positioning, exposure age dating of ice thicknesses, and relative sea level histories. *Geophys. J. Int.* 198, 537–563.
- Barletta, V.R., Bevis, M., Smith, B.E., Wilson, T., Brown, A., Bordoni, A., Willis, M., Khan, S.A., Rovira-Navarro, M., Dalziel, I., et al., 2018. Observed rapid bedrock uplift in Amundsen Sea embayment promotes ice-sheet stability. *Science* 360, 1335–1339.
- Barletta, V.R., Sabadini, R., Bordoni, A., 2008. Isolating the PGR signal in the GRACE data: impact on mass balance estimates in Antarctica and Greenland. *Geophys. J. Int.* 172, 18–30.
- Bevis, M., Kendrick, E., Smalley, R., Dalziel, I., Caccamise, D., Sasgen, I., Helsen, M., Taylor, F., Zhou, H., Brown, A., Raleigh, D., Willis, M., Wilson, T., Konfal, S., 2009. Geodetic measurements of vertical crustal velocity in West Antarctica and the implications for ice mass balance. *Geochem. Geophys. Geosyst.* 10. <https://doi.org/10.1029/2009GC002642>.
- Bonin, J.A., Chambers, D.P., Cheng, M., 2018. Using satellite laser ranging to measure ice mass change in Greenland and Antarctica. *Cryosphere* 12, 71–79.
- Bradley, S.L., Hindmarsh, R.C., Whitehouse, P.L., Bentley, M.J., King, M.A., 2015. Low post-glacial rebound rates in the Weddell Sea due to Late Holocene ice-sheet readvance. *Earth Planet. Sci. Lett.* 413, 79–89.
- Briggs, R., Pollard, D., Tarasov, L., 2013. A glacial systems model configured for large ensemble analysis of Antarctic deglaciation. *Cryosphere* 7, 1949–1970.

- Carlson, A.E., Clark, P.U., 2012. Ice sheet sources of sea level rise and freshwater discharge during the last deglaciation. *Rev. Geophys.* 50. <https://doi.org/10.1029/2011RG000371>.
- Caron, L., Ivins, E., Larour, E., Adhikari, S., Nilsson, J., Blewitt, G., 2018. GIA model statistics for GRACE hydrology, cryosphere, and ocean science. *Geophys. Res. Lett.* 45, 2203–2212.
- Caron, L., Métivier, L., Greff-Lefftz, M., Fleitout, L., Rouby, H., 2017. Inverting glacial isostatic adjustment signal using Bayesian framework and two linearly relaxing rheologies. *Geophys. J. Int.* 209, 1126–1147.
- Chen, J., Wilson, C., Tapley, B., Blankenship, D., Young, D., 2008. Antarctic regional ice loss rates from GRACE. *Earth Planet. Sci. Lett.* 266, 140–148.
- Fleming, K., Tregoning, P., Kuhn, M., Purcell, A., McQueen, H., 2012. The effect of melting land-based ice masses on sea-level around the Australian coastline. *Aust. J. Earth Sci.* 59, 457–467.
- Gomez, N., Latychev, K., Pollard, D., 2018. A coupled ice sheet-sea level model incorporating 3D earth structure: variations in Antarctica during the last deglacial retreat. *J. Climate* 31, 4041–4054.
- Gunter, B., Didova, O., Riva, R., Ligtenberg, S., Lenaerts, J., King, M., Van den Broeke, M., Urban, T., et al., 2014. Empirical estimation of present-day Antarctic glacial isostatic adjustment and ice mass change. *Cryosphere* 8, 743–760.
- Hansen, S., Graw, J., Kenyon, L., Nyblade, A., Wiens, D., Aster, R., Huerta, A., Anandakrishnan, S., Wilson, T., 2014. Imaging the Antarctic mantle using adaptively parameterized P-wave tomography: evidence for heterogeneous structure beneath West Antarctica. *Earth Planet. Sci. Lett.* 408, 66–78. <https://doi.org/10.1016/j.epsl.2014.09.043>.
- Ivins, E.R., James, T.S., Wahr, J., Schrama, E.J.O., Landerer, F.W., Simon, K.M., 2013. Antarctic contribution to sea-level rise observed by GRACE with improved GIA correction. *J. Geophys. Res., Solid Earth* 118, 3126–3141.
- Ivins, E.R., Raymond, C.A., James, T.S., 2000. The influence of 5000 year-old and younger glacial mass variability on present-day crustal rebound in the Antarctic Peninsula. *Earth Planets Space* 52, 1023–1029.
- Kaufmann, G., Wu, P., Ivins, E.R., 2005. Lateral viscosity variations beneath Antarctica and their implications on regional rebound motions and seismotectonics. *J. Geodyn.* 39, 165–181.
- Kendall, R.A., Mitrovica, J.X., Milne, G.A., 2005. On post-glacial sea level – II. Numerical formulation and comparative results on spherically symmetric models. *Geophys. J. Int.* 161, 679–706. <https://doi.org/10.1111/j.1365-246X.2005.02553.x>.
- Lambeck, K., Rouby, H., Purcell, A., Sun, Y., Cambridge, M., 2014. Sea level and global ice volumes from the Last Glacial Maximum to the Holocene. *Proc. Natl. Acad. Sci.* 111, 15296–15303.
- Lloyd, A.J., Wiens, D.A., Zhu, H., Tromp, J., Nyblade, A.A., Aster, R.C., Hansen, S.E., Dalziel, I.W.D., Wilson, T.J., Ivins, E.R., O'Donnell, J.P., 2019. Seismic structure of the Antarctic upper mantle based on adjoint tomography. *J. Geophys. Res., Solid Earth* 124. <https://doi.org/10.1029/2019JB017823>.
- Lorius, C., Raynaud, D., Petit, J.-R., Jouzel, J., Merlivat, L., 1984. Late-glacial maximum-Holocene atmospheric and ice-thickness changes from Antarctic ice-core studies. *Ann. Glaciol.* 5, 88–94.
- Martin-Español, A., Bamber, J.L., Zammit-Mangion, A., 2017. Constraining the mass balance of East Antarctica. *Geophys. Res. Lett.* 44, 4168–4175. <https://doi.org/10.1002/2017GL072937>.
- Martin-Español, A., King, M.A., Zammit-Mangion, A., Andrews, S.B., Moore, P., Bamber, J.L., 2016. An assessment of forward and inverse GIA solutions for Antarctica. *J. Geophys. Res., Solid Earth* 121, 6947–6965. <https://doi.org/10.1002/2016JB013154>.
- Milne, G., Gehrels, W., Hughes, C., Tamisiea, M., 2009. Identifying the causes of sea-level change. *Nat. Geosci.* 2, 471–478. <https://doi.org/10.1038/ngeo544>.
- Mitrovica, J.X., Milne, G.A., Davis, J.L., 2001. Glacial isostatic adjustment on a rotating Earth. *Geophys. J. Int.* 147, 562–578.
- Nield, G.A., Whitehouse, P.L., van der Wal, W., Blank, B., O'Donnell, J.P., Stuart, G.W., 2018. The impact of lateral variations in lithospheric thickness on glacial isostatic adjustment in West Antarctica. *Geophys. J. Int.* 214, 811–824.
- O'Donnell, J., Selway, K., Nyblade, A., Brazier, R., Wiens, D., Anandakrishnan, S., Aster, R., Huerta, A., Wilson, T., Winberry, J., 2017. The uppermost mantle seismic velocity and viscosity structure of central West Antarctica. *Earth Planet. Sci. Lett.* 472, 38–49.
- Peltier, W., Argus, D., Drummond, R., 2015. Space geodesy constrains ice age terminal deglaciation: the global ICE-6G\_C (VM5a) model. *J. Geophys. Res., Solid Earth* 120, 450–487.
- Riva, R.E., Gunter, B.C., Urban, T.J., Vermeersen, B.L., Lindenbergh, R.C., Helsen, M.M., Bamber, J.L., van de Wal, R.S., van den Broeke, M.R., Schutz, B.E., 2009. Glacial isostatic adjustment over Antarctica from combined ICESat and GRACE satellite data. *Earth Planet. Sci. Lett.* 288, 516–523.
- Sasgen, I., Martín-Español, A., Horvath, A., Kleemann, V., Petrie, E.J., Wouters, B., Horwath, M., Pail, R., Bamber, J.L., Clarke, P.J., et al., 2018. Altimetry, gravimetry, GPS and viscoelastic modeling data for the joint inversion for glacial isostatic adjustment in Antarctica (ESA STSE project REGINA). *Earth Syst. Sci. Data* 10, 493–523.
- Schrama, E.J., Wouters, B., Rietbroek, R., 2014. A mascon approach to assess ice sheet and glacier mass balances and their uncertainties from GRACE data. *J. Geophys. Res., Solid Earth* 119, 6048–6066.
- Shepherd, A., Ivins, E.R., Geruo, A., Barletta, V.R., Bentley, M.J., Bettadpur, S., Briggs, K.H., Bromwich, D.H., Forsberg, R., Galin, N., et al., 2012. A reconciled estimate of ice-sheet mass balance. *Science* 338, 1183–1189.
- Shepherd, A., Ivins, E., Rignot, E., Smith, B., van den Broeke, M., Velicogna, I., Whitehouse, P., Briggs, K., Joughin, I., Krinner, G., et al., 2018. Mass balance of the Antarctic ice sheet from 1992 to 2017. *Nature* 556, 219–222.
- Small, D., Bentley, M.J., Jones, R.S., Pittard, M.L., Whitehouse, P.L., 2019. Antarctic ice sheet palaeo-thinning rates from vertical transects of cosmogenic exposure ages. *Quat. Sci. Rev.* 206, 65–80. <https://doi.org/10.1016/j.quascirev.2018.12.024>.
- Sośnicka, K., Thaller, D., Jäggi, A., Dach, R., Beutler, G., 2012. Sensitivity of LAGEOS orbits to global gravity field models. *Artif. Satell.* 47, 47–65.
- Stenni, B., Curran, M.A., Abram, N.J., Orsi, A., Goursaud, S., Masson-Delmotte, V., Neukom, R., Goosse, H., Divine, D., Van Ommen, T., et al., 2017. Antarctic climate variability on regional and continental scales over the last 2000 years. *Clim. Past* 13, 1609–1634.
- Stone, J., Balco, G., Sugden, D., Caffee, M., Sass, L., Cowdery, S., Siddoway, C., 2003. Holocene deglaciation of Marie Byrd land, West Antarctica. *Science* 299, 99–102.
- Tapley, B., Watkins, M., Flechtner, F., Reigber, C., Bettadpur, S., Rodell, M., Sasgen, I., Famiglietti, J., Landerer, F., Chambers, D., Reager, J., Gardner, A., Save, H., Ivins, E., Swenson, S., Boening, C., Dahle, C., Wiese, D., Dobslaw, H., Tamisiea, M., Velicogna, I., 2019. Contributions of GRACE to understanding climate change. *Nat. Clim. Change* 9, 358–369.
- Thomas, E.R., Melchior Van Wessem, J., Roberts, J., Isaksson, E., Schlosser, E., Fudge, T.J., Valletonga, P., Medley, B., Lenaerts, J., Bertler, N., et al., 2017. Regional Antarctic snow accumulation over the past 1000 years. *Clim. Past* 13, 1491–1513.
- Velicogna, I., Wahr, J., 2006. Measurements of time-variable gravity show mass loss in Antarctica. *Science* 311, 1754–1756.
- Velicogna, I., Wahr, J., 2013. Time-variable gravity observations of ice sheet mass balance: precision and limitations of the GRACE satellite data. *Geophys. Res. Lett.* 40, 3055–3063. <https://doi.org/10.1002/grl.50527>.
- Wahr, J., Wingham, D., Bentley, C., 2000. A method of combining ICESat and GRACE satellite data to constrain Antarctic mass balance. *J. Geophys. Res., Solid Earth* 105, 16279–16294.
- van der Wal, W., Whitehouse, P.L., Schrama, E.J., 2015. Effect of GIA models with 3D composite mantle viscosity on GRACE mass balance estimates for Antarctica. *Earth Planet. Sci. Lett.* 414, 134–143.
- Whitehouse, P.L., Bentley, M.J., Milne, G.A., King, M.A., Thomas, I.D., 2012. A new glacial isostatic adjustment model for Antarctica: calibrated and tested using observations of relative sea-level change and present-day uplift rates. *Geophys. J. Int.* 190, 1464–1482.
- Whitehouse, P.L., Gomez, N., King, M.A., Wiens, D.A., 2019. Solid Earth change and the evolution of the Antarctic ice sheet. *Nat. Commun.* 10, 503. <https://doi.org/10.1038/s41467-018-08068-y>.
- Wieczorek, M.A., Meschede, M., Oshchepkov, I., Sales de Andrade, E., heroxbd, 2016. SHOTOOLS: Version 4.0. <https://doi.org/10.5281/zenodo.206114>.
- Willen, M.O., Horwath, M., Schröder, L., Groh, A., Ligtenberg, S.R.M., Kuipers Munneke, P., van den Broeke, M.R., 2019. Sensitivity of inverse glacial isostatic adjustment estimates over Antarctica. *Cryosphere Discuss.* 2019, 1–27. <https://doi.org/10.5194/tc-2019-95>.
- Winstrup, M., Valletonga, P., Kjær, H.A., Fudge, T.J., Lee, J.E., Riis, M.H., Edwards, R., Bertler, N.A.N., Blunier, T., Brook, E.J., Buizert, C., Ciobanu, G., Conway, H., Dahl-Jensen, D., Ellis, A., Emanuelsson, B.D., Hindmarsh, R.C.A., Keller, E.D., Kurbatov, A.V., Mayewski, P.A., Neff, P.D., Pyne, R.L., Simonsen, M.F., Svensson, A., Tuohy, A., Waddington, E.D., Wheatley, S., 2019. A 2700-year annual timescale and accumulation history for an ice core from Roosevelt Island, West Antarctica. *Clim. Past* 15, 751–779. <https://doi.org/10.5194/cp-15-751-2019>.